Rare Metal Materials and Engineering
Volume 54, Issue 11, November 2025
Available online at www.rmme.ac.cn

Science Press

Cite this article as: Liang Xiangfeng, Wu Jili, Kai Xizhou, et al. Creep Fracture Behavior and Mechanism of a New Nickel-Based Single-Crystal Superalloy[J]. Rare Metal Materials and Engineering, 2025, 54(11): 2795-2801. DOI: https://doi.org/10.12442/j.issn.1002-185X.20240632.

ARTICLE

Creep Fracture Behavior and Mechanism of a New Nickel-Based Single-Crystal Superalloy

Liang Xiangfeng[1], Wu Jili[1], Kai Xizhou[1], Dai Yong[2], Shi Changkun[2], Zhao Yutao[1]

[1] School of Materials Science & Engineering, Jiangsu University, Zhenjiang 212013, China; [2] Anhui Yingliu Electromechanical Co., Ltd, Liuan 237299, China

Abstract: A new type of nickel-based single-crystal superalloy was subjected to creep performance test, microstructure observation, and composition analysis under the condition of 1100 °C/140 MPa. The variation characteristics of the creep rate during the creep fracture process and the microstructure evolution before and after creep were investigated, thereby revealing the creep fracture mechanism of the new nickel-based single-crystal superalloy. The results indicate that the creep life of the alloy is 104.5 h, and the strain can reach 33.58%. The creep rate decreases first, then increases, and finally tends to be stable until fracture. At the initial stage of creep, the creep rate decreases first, then rises and finally decreases again with time. Furthermore, the creep fracture microstructure is composed of dimples and tearing edges without obvious slip planes. Oxides and recrystallized structures exist inside the fracture surface, and the voids inside the fracture are elongated and perpendicular to the stress axis, showing a fracture mechanism of microcrack accumulation.

Key words: nickel-based single-crystal superalloy; creep rate; fracture characteristics; creep mechanisms

1 Introduction

Nickel-based single-crystal superalloys are the preferred materials for manufacturing turbine blades in aerospace engines and gas turbines[1–6]. However, these blades often experience creep damage due to centrifugal forces, which is one of the main causes of failure[7–10]. Therefore, the high-temperature creep behavior of single-crystal superalloys has attracted significant attention. To meet the increasing demands for engine efficiency, turbine inlet temperatures are continuously rising, leading to the gradual application of second-generation nickel-based single-crystal superalloys with better high-temperature resistance[11–14]. Thus, studying the creep behavior of nickel-based single-crystal superalloys at 1100 ℃ is of great significance. It is generally believed that at high temperatures, dislocation cutting of the γ' phase in the rafted structure reduces the creep resistance, resulting in an increasing creep rate[15–19]. Additionally, Reed et al[20] proposed that internal casting pores and voids induced by topologically close-packed phases at 1100 ℃/100 MPa are responsible for fracture. Tian et al[21] suggested that in the later stage of creep at 1100 ℃, continuous dislocation cutting of the γ' phase leads to twisting and shearing of the γ/γ' interfaces, resulting in the formation of micropores at the interface, and subsequent crack formation, and alloy failure. However, they did not consider the influence of pre-existing casting pores on creep fracture. Furthermore, the role of oxidation in creep fracture cannot be ignored. This is because surface oxide layers and crack propagation into the interior will reduce the effective load-bearing area and accelerate fracture[22–26]. However, the previous studies on creep fracture mechanisms of rod-shaped specimens have rarely taken oxidation into account. Therefore, this study investigates the creep fracture mechanisms of a second-generation nickel-based single-crystal superalloy at 1100 ℃, aiming to provide a theoretical foundation for the safe and stable use of nickel-based single-crystal turbine blades.

2 Experiment

The material used in this study is a novel nickel-based

Received date: October 25, 2024
Foundation item: China Postdoctoral Science Foundation General Project (2024M760034); Postdoctoral Research Programs of Anhui Province (2024A774)
Corresponding author: Liang Xiangfeng, Ph. D., School of Materials Science & Engineering, Jiangsu University, Zhenjiang 212013, P. R. China, E-mail: lxf@ujs.edu.cn

single-crystal superalloy, which is meticulously designed and developed by our research group. The composition is detailed in Table 1. Directional solidification was conducted using a VIDF-10 model single-crystal furnace, employing the helical crystal selection method at a withdrawal rate of 3.0 mm/min to produce single-crystal castings with dimension of Φ15 mm× 210 mm. Subsequently, the crystal orientation was assessed via electron backscatter diffractometer (EBSD) to ensure that the deviation from the [001] direction remained below 6°, as illustrated in Fig.1. Following this, the single-crystal test rods underwent heat treatment in a Carbolite RHF14/35 high-temperature furnace according to the following schedule: 1300 ℃/4 h/air cooling (AC)+1330 ℃/8 h/AC+1180 ℃/4 h/AC+870 ℃/24 h/AC. The treated single-crystal rods were subsequently machined into creep specimens as illustrated in Fig. 2. Creep testing was performed on an electronic high-temperature creep and durability testing machine (model CTM504-B1) at an experimental temperature of 1100 ℃ with temperature fluctuations maintained within ±5 ℃ under a stress of 140 MPa.

Following the completion of the creep fracture experiment, the specimens underwent a series of preparatory procedures including cleaning, embedding, grinding, and polishing. Subsequently, they were subjected to etching with a solution consisting of 20 mL HNO_3, 100 mL HCl, 7 g $FeCl_3$, 5 g $CuCl_2$, and 100 mL H_2O. The fracture surfaces of the specimens were then examined under both a stereomicroscope and a scanning electron microscope (SEM) for detailed microstructural analysis.

Table 1 Chemical composition of nickel-based single-crystal superalloy (wt%)[27]

Cr	Co	Ti	Al	W	Re	Mo	Ta	Hf	Nb	Ni
3.0	9.5	0.3	6.0	9.0	3.5	1.1	6.0	0.1	0.4	Bal.

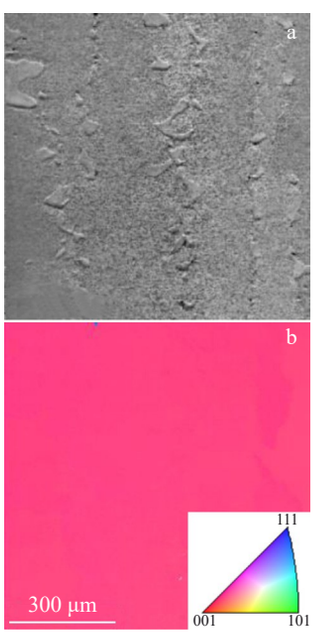

Fig.1 Microstructure and EBSD diagram of nickel-based single-crystal superalloy

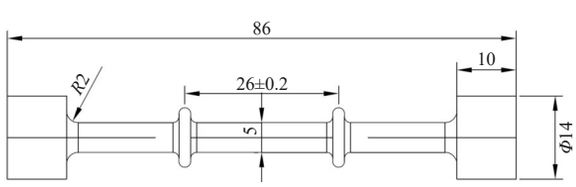

Fig.2 Schematic diagram of dimension of creep specimen

3 Results and Discussion

3.1 Analysis of high-temperature and low-stress creep curve

Fig. 3a shows the creep curve of the nickel-based single-crystal superalloy at 1100 ℃/140 MPa. It can be observed that the creep life of the alloy is 104.5 h with a fracture strain of 33.58%. The creep behavior exhibits a typical rafting mechanism, and the creep curve displays three distinct stages: (1) an initial decelerating creep stage characterized by significant work hardening, lasting for approximately 14 h with a deformation of about 2.5%, as indicated by the black arrow in Fig.3a; (2) a steady-state creep stage in the mid-creep period, where the alloy experiences a balance between work hardening and recovery softening, resulting in a longer strain accumulation with relatively smaller strain, occupying around 60% of the total creep life; (3) an accelerated creep stage in the later creep period, characterized by a rapid increase in strain, lasting for approximately 20 h until fracture occurs. Fig. 3b represents the creep rate-strain curve under the condition of 1100 ℃/140 MPa. Within the initial strain range

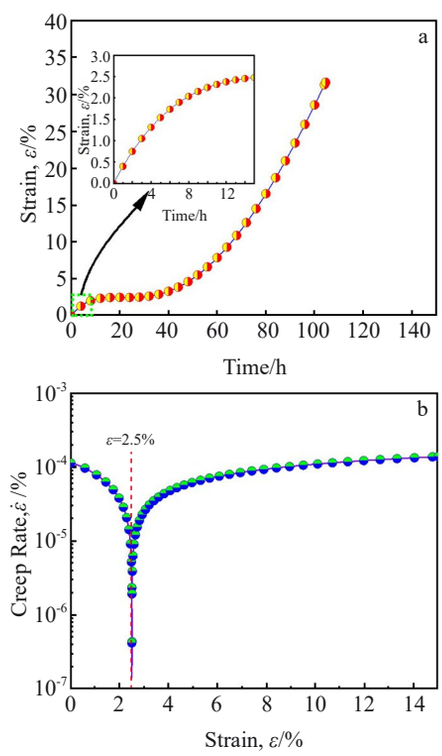

Fig.3 Creep curve (a) and creep rate-strain curve (b) of nickel-based single-crystal superalloy under the condition of 1100 ℃/140 MPa

of 2.5%, the creep rate shows a decreasing trend, corresponding to the decelerating creep stage observed in Fig. 3a. After reaching the minimum point, the creep curve enters the steady-state creep stage, and the creep rate increases with increasing strain, indicating the transition to the accelerated creep stage.

Fig. 4 presents the creep rate-time curve at 1100 °C/140 MPa. It can be observed that within the initial 22 h of creep, the creep rate undergoes three relatively distinct sub-stages: an initial decrease, followed by a rebound, and then another decrease. At the onset of creep, the native dislocations within the γ phase start sliding along the channels under the influence of internal and external stresses. The dislocation density gradually rises, and the stress within the horizontal γ channels starts to decline to alleviate the increasing dislocation density, as depicted in stage A of Fig.4. As the dislocation density continues to escalate, dislocations in local areas begin to entangle to a certain extent, resulting in an enhancement of local creep resistance and a further reduction in strain rate. The creep resistance τ_{Dis} in this portion can be expressed as follows:

$$\tau_{Dis} = \alpha\mu|\boldsymbol{b}|\sqrt{\rho} \quad (1)$$

where α is a material constant; μ is the shear modulus, $\boldsymbol{b}$ is the Burgers vector; ρ is the dislocation density[28].

As creep proceeds, the elements that form the γ phase in the corner regions of the γ' phase accelerate diffusion along the effective diffusion channels provided by dislocations under the effect of the higher von Mises criterion, causing instability in the corner regions of the γ' phase. Partial regions even undergo a certain degree of coalescence, which reduces the creep resistance of the single-crystal superalloy. Under this factor, the creep rate increases with creep time, as shown in stage B of Fig. 4. With the continuous progress of creep, higher-density dislocations interact with each other, and the dislocation network gradually forms. Simultaneously, the coalescence behavior of the γ' phase persists with the increase in dislocation density. When creep reaches 22 h, the rafting of the γ' phase and the dislocation network have been completed, leading to another reduction in creep rate, as shown in stage C of Fig.4.

When entering the steady-state creep, with the accumulation of plastic strain, dislocations in local areas continuously accumulate, and the generated back stress also steadily increases. The dislocation network in the local areas gradually loses its regularity, as shown in stage II of Fig. 4. When entering the final accelerated creep stage (stage III in Fig. 4), a large number of dislocations shear into the γ' phase from regions with higher internal stresses, resulting in a rapid increase in creep rate. This causes an increase in pore size within the creep microstructure of the single-crystal superalloy, and crack propagation accelerates plastic deformation until fracture.

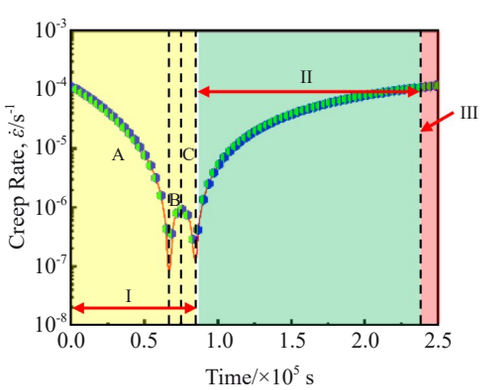

Fig.4 Creep rate-time curve under the condition of 1100 °C/140 MPa

3.2 Analysis of fracture morphology and microstructure

Fig.5a presents a side image of the creep fracture surface of the nickel-based single-crystal superalloy. It can be observed that there is an obvious necking phenomenon near the fracture, suggesting that plastic deformation occurs in the specimen during the creep process. Meanwhile, numerous stepped transverse cracks perpendicular to the stress axis are generated on the outer surface of the fracture. From the side view, the fracture surface is concave. Fig. 5b depicts a cross-sectional image of the sample fracture surface, which is mainly composed of small circular ductile dimples, and no distinct slip planes are observed, indicating that the fracture process involves only plastic deformation and no shear fracture along the slip planes. This precisely explains the reason for the rapid increase in strain in the third stage in Fig. 3a. Fig. 5c illustrates the longitudinal microstructure adjacent to the fracture surface. It is evident that the morphology of the γ' phase in this region exhibits significant distortion and pronounced directional coarsening. This phenomenon can be attributed to the combined effects of elevated temperature and applied stress, which induce deformation in the specimen. The longitudinal tensile stress modifies the stress distribution surrounding the originally cubic γ' phase, leading to lattice distortion in both γ and γ' phases. Consequently, a substantial accumulation of dislocations occurs at this site, resulting in an increase in alloy

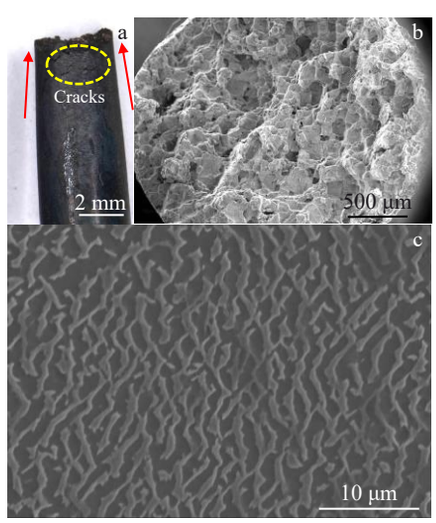

Fig.5 Creep fracture morphologies of nickel-based single-crystal superalloy: (a) side image; (b) cross-sectional image; (c) longitudinal image

strain energy at the interface between these two phases and promoting diffusion of alloying elements. This process ultimately facilitates the development of a raft-like microstructure following directional coarsening of the γ' phase.

Fig. 6a illustrates the local morphology of the cross-section of the creep fracture. Evidently, there are distinct microvoids at the center of the dimples, surrounded by a relatively flat area. Prominent tearing edges are observed at the edges, connecting with adjacent dimples. This indicates that the necking and fracture phenomena observed in the specimen during the accelerated creep stage are attributed to the interconnection of microvoids within the material, forming microcracks. These microcracks propagate and converge along the rafting direction of the γ' phase, forming larger cracks. The entire fracture process does not exhibit slippage along a specific crystal orientation. Hence, it can be inferred that nickel-based single-crystal superalloys can enhance their creep life by eliminating internal microvoids. Fig. 6b presents partial morphology of the longitudinal section of the fracture containing microvoids. The depth of the microvoids significantly exceeds their width, and a dense layer of irregularly shaped oxides forms on the inner surface of the voids. The morphology of these oxides is depicted in Fig. 6c. The elemental analysis results obtained by energy dispersive spectroscope (EDS) reveal that the primary components are metal oxides containing Ni, Cr, Al, Co, Ti, etc. This also suggests that the creep fracture behavior of the alloy is influenced not only by temperature and load but also by material oxidation.

Fig. 7a presents the longitudinal section morphology of the creep fracture surface. The yellow dashed line represents the orientation of the fracture surface cross-section, which is nearly perpendicular to the stress axis. At a position approximately 400 μm perpendicular to the yellow dashed line, there exists a fracture step (indicated by the blue dashed line in Fig. 7a). As depicted in Fig. 7b, a large number of microcracks (indicated by the blue arrows) accumulate at this location, which serves as a potential position for the fracture surface. The directions of these microcracks are nearly parallel, suggesting that the cracks produced in different cross-sections (perpendicular to the stress axis) near the fracture surface are relatively dense. As shown in Fig. 7d, during the creep process, the microcracks are on the verge of convergence. Once the cracks within one or more cross-sections complete the accumulation and penetrate the specimen, the two sides of the cross-section separate, forming the fracture surface. Fig. 7c is an enlarged image of the crack corner indicated by the black circle in Fig. 7a. It can be observed from Fig. 7c that cellular recrystallization structure in area B consisting of fine irregular block-shaped γ' phase emerges at the crack corner, which is protrusive and exhibits cracking. This is attributed to the significant plastic deformation near the fracture surface, high accumulation of strain energy, and the occurrence of recrystallization at 1100 ℃. The composition of this structure is shown in Fig. 7e. Area C in Fig. 7c represents the outer surface of the creep specimen, and an oxide layer with a thickness of up to 50 μm forms on the specimen surface. The morphology of area C is completely different from the recrystallization structure of area B. The area C is relatively dense and flat, and its composition is presented in Fig. 7f. Both area A and area B contain oxides of Cr and Al. Due to the poor density of oxides in area B, which is prone to spalling, it will accelerate the oxidation damage of the alloy and deteriorate the creep performance.

3.3 Evolution of pore morphology

Fig. 8 presents the various scanning positions of the

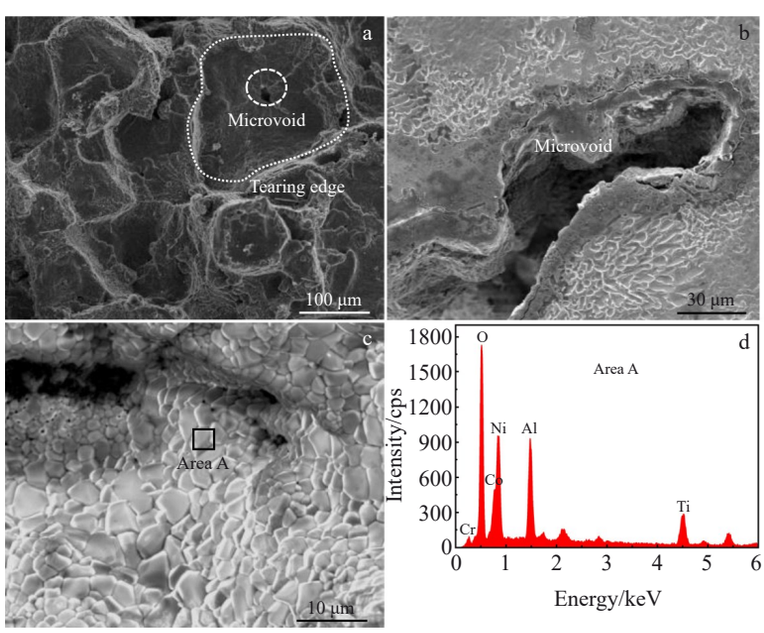

Fig.6 Creep fracture morphologies of nickel-based single-crystal superalloys: (a) local cross-sectional morphology, (b) longitudinal section of microvoids, and (c) surface oxides; (d) EDS result of area A marked in Fig.6c

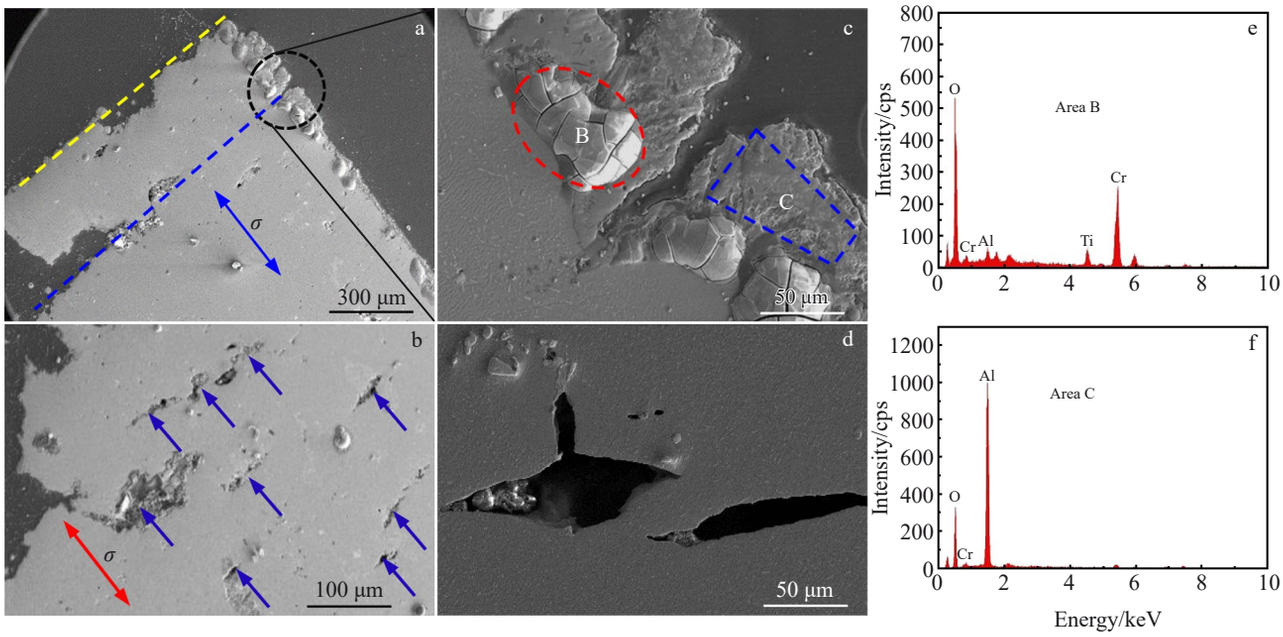

Fig.7 Microstructural morphologies near the creep fracture surface (a–d) of nickel-based single-crystal superalloys: (a, c) longitudinal section morphology; (b) microcracks; (d) microcrack propagation; EDS results of area B (e) and C (f) marked in Fig.7c

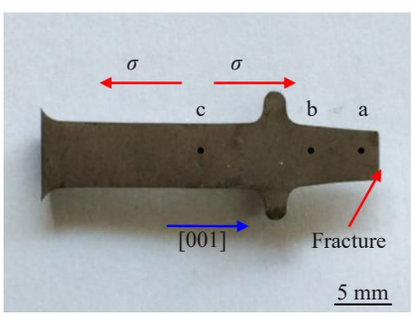

Fig.8 Locations of observation points on fracture surface of creep specimen

fractured specimen. The microstructural morphologies at points a, b, and c are illustrated in Fig. 9. The results demonstrate that as the distance from the fracture location decreases, the morphology of the voids exhibits a stepped change. At a distance of 15 mm from the fracture surface, as depicted in Fig. 9c, the void morphology appears as gourd-shaped or irregular, and the long side of the void is approximately perpendicular to the stress axis. Whereas at a distance of 7 mm from the fracture surface, as shown in Fig.9b, the void assumes a quasi-elliptical shape. At a distance of 2 mm near the fracture surface, as indicated in Fig. 9a, the void takes on a large elongated shape, and the long axis of the elongated void is perpendicular to the stress axis. It is widely acknowledged that in the as-cast microstructure of nickel-based single-crystal superalloys, the majority of voids assume irregular shapes. After heat treatment, the voids exhibit a spheroidizing trend, while during the creep process, they tend towards quasi-elliptical forms[29–31]. Epishin et al[32] have indicated that under the creep conditions of high temperature and low stress, voids are prone to presenting hexagonal and polyhedral configurations. The polyhedral voids are mostly octahedral or dodecahedral. This is attributed to the fact that under the combined effects of the temperature field and stress field, a considerable number of vacancies within the alloy

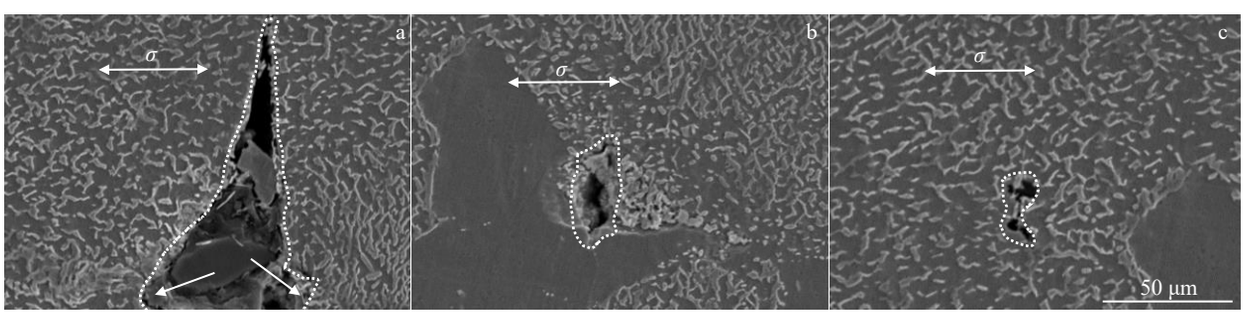

Fig.9 Microstructural morphologies of voids at different locations in fractured specimen with a distance of 2 mm (a), 7 mm (b), and 15 mm (c) from fracture surface

gradually migrate and release towards the surface. The casting microvoids remaining from the casting process precisely offer the vacancies a space for movement, thereby resulting in an increase in size of the voids. On the other hand, the aggregation of vacancies at the surface of voids is more prone to the {111} plane rather than the {001} plane, thereby causing negative growth of the crystal at the void location. Eventually, the {001} plane around the void is retained, and the morphology of the void becomes closer to hexagonal, octahedral, and dodecahedral shapes. Consequently, a large number of elliptical-like voids can be observed in both longitudinal and cross-sectional views, as depicted in Fig. 9b. Moreover, in the microstructure far from the fracture surface, irregularly shaped void structures can be discovered. These might be small voids generated during the casting or heat treatment processes, which do not significantly increase in size during the creep process, and their crystallographic orientation characteristics are not obvious, as shown in Fig. 9c. It is noteworthy that near the fracture position, although the voids appear in elongated shapes, they are still associated with the original spherical pores, as indicated by the white arrow in Fig. 9a. This is due to the necking that occurs near the fracture of specimen after creep fracture. As the distance from the fracture surface gets closer, the tensile stress applied to specimen gradually increases.

4 Conclusions

1) The creep life of the novel nickel-based single-crystal superalloy is 104.5 h under the condition of 1100 °C/140 MPa with a strain of 33.58%. The creep rate decreases first, then increases, and finally tends to be stable until fracture with the overall strain.

2) During the initial 22 h of creep for the novel nickel-based single-crystal superalloy, the creep rate shows three relatively obvious sub-stages with time, namely, a decrease followed by a rise and then another decrease.

3) The creep fracture microstructure of the novel nickel-based single-crystal superalloy is composed of dimples and tearing edges without obvious slip planes. Oxides and recrystallized structures exist inside the fracture surface, the voids within the fracture are elongated, and the fracture mechanism is presented as microcrack accumulation type.

References

1 Pang L, Zhang Z X, Kong L W *et al. Journal of Alloys and Compounds*[J], 2023, 944: 169224

2 Zhang Jingang, Chen Xing, Li Zhen *et al. Rare Metal Materials and Engineering*[J], 2023, 52(6): 1985

3 Zhao G Q, Tian S G, Zhang S K *et al. Progress in Natural Science: Materials International*[J], 2019, 29: 210

4 Liang X F, Zhao Y T, Ma D *et al. Materials and Manufacturing Processes*[J], 2017, 32: 1887

5 Zhang Z P, Liu J D, Qiu K Q *et al. Metals and Materials International*[J], 2023, 29: 444

6 Rai R K. *Materials Science and Technology*[J], 2023, 39: 714

7 Cui Zhuang, Liu Manping, Zeng Ying *et al. Rare Metal Materials and Engineering*[J], 2024, 53(8): 2375 (in Chinese)

8 Svetlov I L, Petrushin N V, Epishin A I *et al. Physics of Metals and Metallography*[J], 2022, 123: 831

9 Cheng Yuan, Zhao Xinbao, Yue Quanzhao *et al. Rare Metal Materials and Engineering* [J], 2023, 52(7): 2599 (in Chinese)

10 Wang Y L, Zhuo L C, Yin E H *et al. Materials Science and Technology*[J], 2022, 38: 836

11 Ai X, Shi L J, Luo F H *et al. Engineering Fracture Mechanics*[J], 2023, 284: 109262

12 Zhang Jingang, Liu Xinling, Chen Xing *et al. Rare Metal Materials and Engineering*[J], 2024, 53(9): 2458

13 Tan Z H, Wang X G, Du Y L *et al. Metals and Materials International*[J], 2022, 28: 1599

14 Kang M D, Wang J, Wei X *et al. Materials Science and Technology*[J], 2020, 36(18): 1980

15 Wei X, Ai X, Wang J *et al. Crystals*[J], 2022, 12(5): 592

16 Taylor P L, Conduit G. *Computational Materials Science*[J], 2022, 201: 110916

17 Liang X F, Wu J, Zhao Y. *Metals and Materials International*[J], 2022, 28: 841

18 Xu Hanyuan, Huang Taiwen, Ai Cheng *et al. Rare Metal Materials and Engineering*[J], 2024, 53(5): 1486 (in Chinese)

19 Xu Weitai, Ma Dexin, Zhao Yunxing *et al. Rare Metal Materials and Engineering*[J], 2022, 51(7): 2637 (in Chinese)

20 Reed R C, Cox D C, Rae C M F. *Materials Science and Engineering A*[J], 2007, 448(1–2): 88

21 Tian Ning, Zhao Guoqi, Meng Tai *et al. Materials Characterization*[J], 2021, 180: 111394

22 Chen J B, Chen J Y, Wang Q J *et al. Acta Materialia*[J], 2022, 232: 117938

23 Du Y L, Yang Y H, Diao A M *et al. Journal of Materials Research and Technology*[J], 2021, 15: 4702

24 Zhang C, Hu W, Wen Z *et al. Materials Science and Engineering A*[J], 2019, 756: 108

25 Li Xiaopeng, Xie Youshui, Huang Yao *et al. Rare Metal Materials and Engineering*[J], 2024, 53(10): 2952 (in Chinese)

26 Mukhtarov S K, Imayev V M, Logunov A V *et al. Materials Science and Technology*[J], 2019, 35: 1605

27 Li Yiling, Jia Zhihong, Tang Wei *et al. Advanced Engineering Materials*[J], 2020, 22(4): 1901151

28 Yue Q Z, Liu L, Yang W C *et al. Journal of Materials Science and Technology*[J], 2019, 35: 752

29 Wang X Y, Wang J J, Zhang C J *et al. Rare Metals*[J], 2021, 40: 2892

30 Zhang Y M, Wen Z X, Pei H Q *et al. Journal of Alloys and Compounds*[J], 2019, 797: 1059

31 Xu J H, Li L F, Liu X G *et al. Materials Characterization*[J], 2022, 187: 111857

32 Epishin A, Link T. *Philosophical Magazine*[J], 2004, 84: 1979

一种新型镍基单晶高温合金蠕变断裂行为及机制

梁向锋[1]，吴继礼[1]，怯喜周[1]，戴　勇[2]，施长坤[2]，赵玉涛[1]
(1. 江苏大学 材料科学与工程学院，江苏 镇江 212013)
(2. 安徽应流集团霍山铸造有限公司，安徽 六安 237299)

摘　要：对一种新型镍基单晶高温合金在1100 ℃/140 MPa的条件下进行了蠕变性能测试、组织形貌观察及成分分析，研究了该合金在蠕变断裂过程中，蠕变速率的变化特点及蠕变前后组织的演变特征，揭示了新型镍基单晶高温合金的蠕变断裂机制。结果表明：该合金的蠕变寿命为104.5 h，应变量可达到33.58%，蠕变速率随应变整体呈现出先递减后递增，最后趋于稳定直至断裂的现象。在蠕变初始阶段，蠕变速率随时间延长呈现先降低再回升而后再降低的现象。此外，蠕变断口组织由韧窝与撕裂棱构成，无明显滑移面，断口内部存在氧化物和再结晶组织，断口内空洞呈现长条状，且垂直于应力轴，表现为微裂纹聚集型断裂机制。

关键词：镍基单晶高温合金；蠕变速率；断裂特性；蠕变机制

作者简介：梁向锋，男，1987年生，博士，江苏大学材料科学与工程学院，江苏 镇江 212013，E-mail：lxf@ujs.edu.cn